Path Correspondence Between Wi-Fi CSI and Radar: A Visibility-Driven Perspective

***Abstract*—Understanding whether Wi-Fi channel state information (CSI) and radar sensing observe the same propagation paths is fundamental to cross-modal RF sensing. Prior work largely attributes discrepancies between modalities to differences in bandwidth and range resolution. In this paper, we revisit this assumption from a path-level perspective and show that cross-modal correspondence is primarily governed by path visibility rather than resolution.**

We introduce the Cross-modal Correspondence Rate (CRC), a metric that quantifies the overlap between dominant propagation paths observed by Wi-Fi CSI and radar. Through large-scale experiments spanning line-of-sight (LOS) and non-line-of-sight (NLOS) conditions, we observe a consistent crossover behavior: lower frequencies achieve higher correspondence at longer ranges, while higher frequencies dominate at short range. Contrary to conventional intuition, this crossover is not explained by resolution, but by whether individual paths remain detectable above the radar noise floor.

To explain this phenomenon, we develop a physics-consistent framework linking wavelength-dependent scattering, received power, and detection. We show that CRC can be expressed as the expected fraction of Wi-Fi-visible paths whose radar signal-to-noise ratio (SNR) exceeds a detection threshold. This leads to a predictive model that quantitatively relates path-level SNR to CRC, validated against direct Sionna RT oracle measurements (Pearson $r = 0.73$, 60/77 GHz NLOS).

Finally, CRC exhibits a sigmoid transition as a function of path detectability, revealing a phase-transition-like behavior where correspondence collapses once SNR falls below the detection boundary. This finding reframes cross-modal sensing as a detectability-limited problem and suggests a shift in system design: ensuring path observability may be more critical than improving resolution.

***Index Terms*—RF sensing, Wi-Fi CSI, radar sensing, monostatic sensing, multipath propagation, cross-modal correspondence, path visibility**

I. Introduction

RF sensing has emerged as a powerful paradigm for environment perception, enabling applications such as human activity recognition, localization, and health monitoring. Among the most widely studied modalities are Wi-Fi channel state information (CSI) [1], [2], [3] and radar [4], [5], both of which exploit radio-frequency signals to infer properties of the surrounding environment.

Despite their shared physical foundation, these two sensing approaches have largely been studied in isolation. Wi-Fi CSI is typically analyzed from a communication perspective, focusing on channel variations and statistical features [6], [7], while radar emphasizes geometric interpretation through explicit range and Doppler estimation [8]. We investigate the following fundamental question:

Under what conditions do Wi-Fi CSI and radar share observable propagation paths, and what governs their correspondence?

This question is not merely academic. If both modalities correspond to the same underlying paths, then insights from one domain could be transferred to the other, enabling unified models and cross-modal system design. Conversely, if they diverge, understanding the conditions under which correspondence fails becomes critical for reliable sensing.

A. Motivation and Challenges

At first glance, both Wi-Fi CSI and radar measure reflections of electromagnetic waves and should therefore capture the same multipath structure. However, practical observations suggest otherwise [9], [10]. Under certain conditions, the two modalities produce inconsistent results, particularly in non-line-of-sight (NLOS) environments and at higher frequencies.

This discrepancy raises several key challenges:

- **Path-level ambiguity:** It is unclear whether CSI peaks correspond to the same physical paths observed by radar.
- **Lack of quantitative metrics:** Existing studies lack a principled way to measure cross-modal correspondence.
- **Unexplained frequency dependence:** Empirical results indicate that sensing performance varies with frequency, but the underlying cause remains poorly understood.

Addressing these challenges requires a unified framework that explicitly models and evaluates cross-modal alignment at the path level.

B. Contributions

In this work, we present a systematic study of path-level correspondence between monostatic Wi-Fi CSI and radar — a question not directly addressed in prior work, which either analyzes each modality independently [1], [4] or transforms CSI into radar-like representations without studying path-level alignment [9], [10]. Our contributions are summarized as follows:

- **Path-level correspondence characterization:** We establish that Wi-Fi CSI and radar are governed

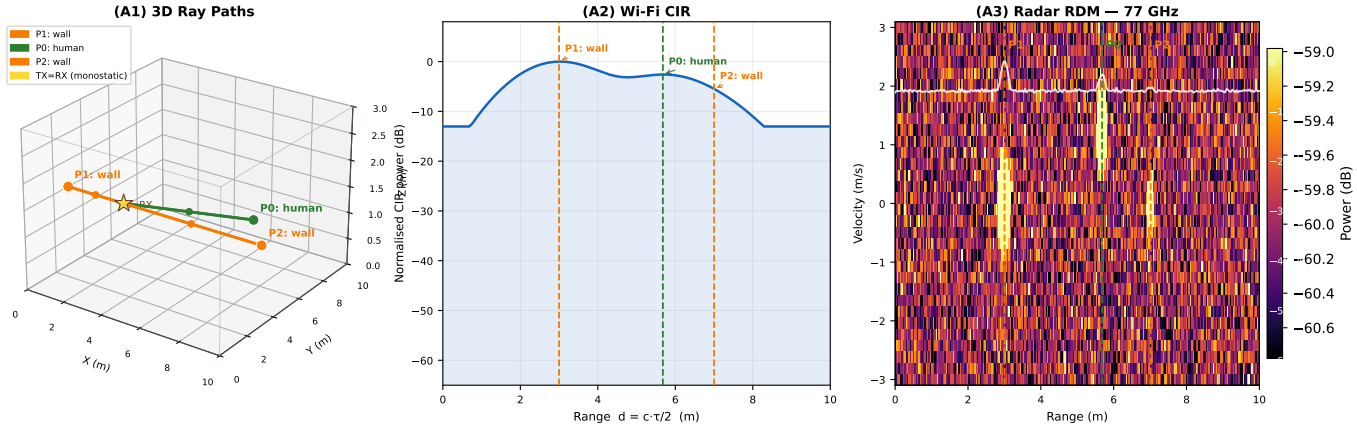

Fig. 1. **Path-level correspondence between Wi-Fi CSI and radar under monostatic sensing.** (A1) 3D ray paths showing dominant propagation components (LOS and reflections). (A2) Wi-Fi CIR (6 GHz) where peaks correspond to path delays. (A3) Radar range-Doppler map (77 GHz) where peaks correspond to the same physical paths.

by the same underlying propagation geometry; their observable path sets coincide when paths are jointly visible under monostatic sensing, forming the basis of cross-modal correspondence (Fig. 1).

- **Cross-modal correspondence metric:** We introduce the Cross-modal Correspondence Rate (CRC), which quantifies the alignment between CSI and radar observations based on shared visible paths.
- **Systematic evaluation across conditions:** Through large-scale simulations, we show that correspondence is condition-dependent, with strong alignment under line-of-sight (LOS) and significant degradation under NLOS conditions (Fig. 2).
- **Frequency-dependent crossover behavior:** We identify a crossover regime in which lower frequencies (e.g., 24 GHz) outperform higher frequencies (60/77 GHz) in terms of correspondence at longer distances (Fig. 3).
- **A visibility-driven perspective:** We show that cross-modal correspondence is governed by path visibility rather than resolution, providing a unified explanation for frequency-dependent sensing behavior. We formalize this with a predictive power-chain model, a formal proposition and detection-limited lemma, and validate it with statistical analysis (Fig. 4), path-level evidence (Fig. 5), and CRC vs SNR analysis (Fig. 7).

C. Key Insight

The central insight of this work is that:

Key Insight. Cross-modal correspondence is governed by *path visibility*, rather than resolution.

While bandwidth determines the ability to resolve paths, correspondence requires that paths are first observable. In realistic environments, especially under NLOS conditions, certain paths become unobservable in one modality due to insufficient signal strength, leading to a reduction in shared paths.

D. Organization

The remainder of this paper is organized as follows. Section III establishes path-level correspondence between CSI and radar. Section IV introduces the CRC metric. Section V analyzes the failure mechanism and presents the visibility-driven model. Section VI presents experimental results, including correspondence maps and crossover behavior. Finally, Section VII concludes the paper and discusses implications for RF sensing system design.

II. Background and Preliminaries

In this section, we briefly review the signal models of Wi-Fi CSI and radar sensing, and establish a unified representation for multipath propagation. This formulation serves as the foundation for the path-level correspondence analysis in Section III.

A. Multipath Propagation Model

RF signals propagate through the environment via multiple paths due to reflection, scattering, and diffraction. Each path can be characterized by a propagation delay τ_p and a complex amplitude a_p.

The received signal can therefore be modeled as a superposition of multipath components:

$$y(t) = \sum_{p \in \mathcal{P}} a_p x(t - \tau_p), \tag{1}$$

where $\mathcal{P}$ denotes the set of propagation paths.

This representation is shared across both communication and radar sensing systems, providing a common physical basis for analysis.

B. Wi-Fi CSI Representation

In Wi-Fi systems, the channel state information (CSI) characterizes the frequency response of the wireless channel. It can be expressed as:

$$H(f) = \sum_{p \in \mathcal{P}} a_p \exp(-j2\pi f \tau_p), \tag{2}$$

where f denotes frequency.

By applying an inverse Fourier transform, the channel impulse response (CIR) can be obtained, where peaks correspond to multipath delays.

C. Radar Range Representation

In radar sensing, the received signal is processed to estimate the range of reflecting objects. Each propagation path produces a peak in the range profile at:

$$R_p = \frac{c\tau_p}{2}, \tag{3}$$

where c is the speed of light.

Thus, radar directly measures propagation delay in the spatial domain.

D. Monostatic Configuration

In this work, we focus on the monostatic configuration, where the transmitter and receiver are co-located.

Under this setting, both Wi-Fi CSI and radar observe round-trip propagation paths. This eliminates geometric asymmetry and enables a direct mapping between CSI delay and radar range.

While this work focuses on the monostatic configuration for clarity, the visibility-driven interpretation extends to general bistatic and multi-static settings, where path observability remains the key limiting factor.

E. Visibility of Propagation Paths

A propagation path p is observable in a given modality if its received power exceeds the system detection threshold:

$$P_{\text{rx}}(p) > P_{\text{noise}} + \gamma, \tag{4}$$

where P_{noise} is the noise floor and γ is a system-dependent detection margin. Thus, path visibility is fundamentally governed by the signal-to-noise ratio (SNR), which depends on transmit power, propagation loss, and frequency-dependent scattering.

Let $\mathcal{P}_{\text{CSI}}$ and $\mathcal{P}_{\text{radar}}$ denote the sets of observable paths in Wi-Fi CSI and radar, respectively. In practice, these sets may differ due to frequency-dependent attenuation, scattering properties, and system sensitivity.

This notion of path visibility will play a central role in understanding cross-modal correspondence in later sections.

While radar visibility is modeled using an explicit detection threshold, Wi-Fi CSI measurements also implicitly involve a detection floor determined by receiver sensitivity and channel estimation noise. In this work, Wi-Fi is treated as the reference modality because, at sub-6 GHz frequencies, it typically exhibits higher robustness to path-loss attenuation and richer multipath observability compared to mmWave radar. However, the proposed CRC framework does not depend on this asymmetry: CRC can equivalently be defined with radar as the reference, and the visibility-driven conclusions remain consistent under either normalization.

F. Related Work

Wi-Fi CSI sensing. Wi-Fi CSI has been widely used for device-free sensing, including gesture recognition, activity recognition, localization, and vital-sign monitoring. Early systems such as WiSee [1], CARM [2], Widar [6], SpotFi [3], and mD-Track [7] demonstrate that commodity Wi-Fi signals contain rich motion, location, and multipath information. However, these works primarily study Wi-Fi as a standalone sensing modality, focusing on feature extraction, localization, or tracking, rather than analyzing whether CSI paths correspond to paths observed by radar.

Wi-Fi range-Doppler sensing. Recent work has pushed Wi-Fi sensing closer to radar-like processing by extracting range and Doppler information from commodity Wi-Fi CSI. LiveSense [10] transforms COTS Intel Wi-Fi NICs into real-time range-Doppler sensors, while RF-DS [11] performs range-filtered Doppler processing for human presence detection on commodity laptops. Related work also extracts range-Doppler information of moving targets from monostatic Wi-Fi CSI using commercial Intel AX211 hardware [9]. These works are highly relevant because they show that Wi-Fi CSI can be represented in radar-like domains. However, they focus on signal processing and system realization, not on the path-level question of when and why Wi-Fi CSI and radar share observable propagation paths.

Radar and RF-based human sensing. Radar and dedicated RF sensing systems provide explicit geometric measurements through range, Doppler, and angle estimation. Systems such as WiTrack [4] and Vital-Radio [8] demonstrate device-free motion tracking and vital-sign sensing using radio reflections. RF-Pose [5] further shows that radio signals can support through-wall human pose estimation using learned representations. These works demonstrate the sensing capability of RF reflections, but generally operate within a single modality and do not quantify correspondence between Wi-Fi CSI and radar.

Cross-modal and multi-modal RF sensing. Recent work has explored knowledge transfer and fusion across different RF sensing modalities. RF Genesis [12] uses simulation-based data synthesis and generative diffusion models to enable zero-shot generalization of mmWave sensing, demonstrating that radar-domain representations can be synthesized from RF channel simulations. These works highlight the potential of cross-modal reasoning but do not study whether the underlying propagation paths are physically aligned across modalities — the question we address.

Ray tracing and propagation modeling. Ray-tracing simulators and propagation models provide path-level descriptions of wireless channels, including delay, amplitude, reflection, scattering, and material interactions. Tools such as Sionna RT [13] and Wireless InSite [14] support physically grounded simulation of multipath propagation and have been used for wireless channel and digital-twin

analysis. These tools enable path-level observability, but prior work has not used them to systematically compare Wi-Fi CSI and radar correspondence.

Gap in prior work. Prior work establishes that Wi-Fi CSI can sense human motion, that radar can extract geometric structure, and that Wi-Fi can even be processed into radar-like range-Doppler representations. However, existing studies either analyze each modality independently or fuse modalities at the feature level. Recent Wi-Fi range-Doppler systems demonstrate that CSI can be transformed into radar-like representations; however, representation equivalence does not imply path-level correspondence. Cross-modal approaches such as RF Genesis [12] show that multi-modal transfer is feasible but rely on learned mappings rather than studying physical path alignment. Furthermore, while the importance of frequency selection in radar design is well-recognized, the impact of frequency on cross-modal path correspondence — and in particular the counterintuitive advantage of lower frequencies under NLOS long-range conditions — has not been studied. To the best of our knowledge, no prior work systematically studies the conditions under which Wi-Fi CSI and radar share observable propagation paths, nor provides a quantitative metric for path-level cross-modal correspondence. This gap motivates our CRC framework and the visibility-driven analysis in this paper.

G. Summary

Both Wi-Fi CSI and radar are governed by the same multipath propagation model, but differ in representation and observability. This shared structure enables path-level comparison across modalities, while differences in path visibility motivate a systematic analysis of cross-modal correspondence. This perspective forms the foundation for the correspondence framework developed in the following sections.

III. Path-Level Correspondence Between Wi-Fi CSI and Radar

In this section, we establish the fundamental relationship between Wi-Fi CSI and radar observations. We show that, under monostatic sensing, both modalities are governed by the same underlying propagation geometry — while their observable path sets may differ due to frequency-dependent visibility, the geometry that determines path delays is shared, enabling a direct mapping between CSI delay and radar range.

A. Monostatic CSI Formulation

We consider a monostatic sensing configuration, where the transmitter and receiver are co-located. Under this setting, the Wi-Fi CSI takes the same form as in Section II-B, with each delay τ_p now representing a round-trip path, consistent with radar sensing. In simulation, the monostatic setting is implemented by co-locating TX and RX at the same position; this controlled abstraction removes bistatic geometry effects and isolates visibility-driven correspondence.

B. Radar Signal Model

In radar sensing, the received signal is also composed of reflected multipath components. After range processing, each path produces a peak at range $R_p = c\tau_p/2$ (Section II-C), directly mapping propagation delay to physical distance.

Thus, both CSI and radar measurements derive from the same underlying propagation geometry $\mathcal{P}$, differing in representation (frequency-domain response vs. range profile) and in which subset of paths is observable at each modality and frequency.

C. Path-Level Correspondence

The above formulation implies a direct mapping between CSI delay and radar range:

$$\tau_p \longleftrightarrow R_p. \tag{5}$$

Therefore, each peak in the CSI-derived channel impulse response (CIR) corresponds to a physical path that should also appear in the radar range profile, provided that the path is observable in both modalities.

Fig. 1 illustrates this correspondence. The same dominant paths (e.g., line-of-sight and wall reflections) appear consistently in both CSI and radar representations, confirming that the two modalities capture the same underlying propagation geometry.

D. Conditions for Correspondence

While the mapping above establishes a theoretical correspondence, it relies on an important condition: the path must be observable in both modalities.

In practice, a path is observable only if its received signal strength exceeds the detection threshold of the sensing system. Let $\mathcal{P}_{\text{CSI}}$ and $\mathcal{P}_{\text{radar}}$ denote the sets of observable paths in Wi-Fi CSI and radar, respectively. Then, path-level correspondence is defined over the intersection:

$$\mathcal{P}_{\text{shared}} = \mathcal{P}_{\text{CSI}} \cap \mathcal{P}_{\text{radar}}. \tag{6}$$

This observation highlights that correspondence is not guaranteed by geometry alone, but depends on the visibility of paths across modalities.

E. Summary

In summary, Wi-Fi CSI and radar share a common physical foundation: both are governed by the same underlying propagation geometry under monostatic sensing. However, their observable path sets may differ, and correspondence between the two modalities is conditioned on path visibility.

This distinction motivates the need for a quantitative measure of correspondence, which we introduce in the next section.

IV. Cross-Modal Correspondence Metric

Building on the path-level correspondence established in Section III, we introduce a quantitative metric to evaluate the alignment between Wi-Fi CSI and radar observations. Our goal is to measure correspondence at the level of physical propagation paths, rather than signal similarity.

A. Problem Formulation

Let $\mathcal{P}_{\text{CSI}}$ and $\mathcal{P}_{\text{radar}}$ denote the sets of observable paths in Wi-Fi CSI and radar, respectively, and let $\mathcal{P}_{\text{shared}} = \mathcal{P}_{\text{CSI}} \cap \mathcal{P}_{\text{radar}}$ denote the set of paths visible in both modalities.

Given that correspondence is defined over shared visible paths, a suitable metric must:

- operate at the path level,
- account for partial matches,
- be robust to noise and minor estimation errors.

B. Top-K Path Selection

In practice, not all paths contribute equally to sensing. We therefore restrict evaluation to the top-K dominant paths ranked by received power.

Let $\mathcal{P}_{\text{CSI}}^{(K)}$ denote the top-K Wi-Fi-visible paths. These paths form the reference set against which radar observations are compared. In this work, we use $K = 3$ by default, and verify robustness to $K \in \{1, 3, 5\}$.

As a physics-grounded alternative to fixed K, an energy-based selection criterion can be defined as:

$$\mathcal{P}_{\text{CSI}}^{(\eta)} = \{p : P_{\text{rx}}(p) > \eta \cdot P_{\max}\}, \tag{7}$$

where $\eta \in (0, 1)$ is a power threshold relative to the strongest path $P_{\max}$. This formulation ties path selection directly to received power rather than a count heuristic. The fixed-K setting used in this work approximates $\eta \approx 0.1$ across the evaluated datasets; CRC trends are stable under both criteria.

C. CRC (Soft Correspondence)

To capture graded alignment between paths, we define the *Cross-modal Correspondence Rate (CRC)* using a Gaussian kernel over range residuals.

For each path $p \in \mathcal{P}_{\text{CSI}}^{(K)}$, let R_p^{CSI} and R_p^{radar} denote the corresponding ranges. The residual is:

$$\Delta R_p = \left| R_p^{\text{CSI}} - R_p^{\text{radar}} \right|. \tag{8}$$

We define the soft correspondence score as:

$$\text{CRC}_{\text{soft}} = \frac{1}{K} \sum_{p \in \mathcal{P}_{\text{CSI}}^{(K)}} \exp\left(-\frac{\Delta R_p^2}{\sigma_R^2} \right), \tag{9}$$

where $\sigma_R = c/(4B_{\text{radar}}) = \Delta r/2$, with B_{radar} the radar bandwidth and $\Delta r = c/(2B_{\text{radar}})$ the range resolution. Setting $\sigma_R = \Delta r/2$ calibrates the kernel to one half-resolution cell. Since range noise is simulated as $\sigma_{\text{noise}} = 0.2\,\Delta r$, the ratio $\sigma_{\text{noise}}/\sigma_R = 0.4$ is constant across all frequencies, removing any frequency-dependent bias from the metric.

Paths that are not observable in radar contribute zero to the sum.

This formulation provides a continuous measure of alignment that is robust to small estimation errors. This result is robust to the choice of tolerance: since the crossover is driven by binary path disappearance rather than range residuals, it persists under a fixed physical tolerance (e.g., $\delta = 0.5$ m) applied uniformly across all frequencies — confirming that the frequency-dependent trend is not an artifact of bandwidth-dependent kernel widths.

D. CRC (Hard Correspondence)

To provide an interpretable measure of visibility overlap, we also define a hard correspondence metric:

$$\text{CRC}_{\text{hard}} = \frac{|\mathcal{P}_{\text{shared}}^{(K)}|}{|\mathcal{P}_{\text{CSI}}^{(K)}|}, \tag{10}$$

where $\mathcal{P}_{\text{shared}}^{(K)}$ denotes the subset of top-K CSI paths that are also observable in radar within a gate tolerance δ.

Path matching uses nearest-neighbor assignment in the range domain: each CSI path is matched to the closest radar peak within tolerance, and unmatched CSI paths contribute zero. Gate tolerances are set to $\delta_{24} = 0.6$ m for 24 GHz (≈ 2 range cells at 500 MHz bandwidth) and $\delta_{60/77} = 0.1$ m for 60 and 77 GHz (1–3 range cells depending on bandwidth), reflecting the different range resolution at each frequency. In the oracle-based simulation, path ranges and amplitudes are provided directly by the ray-tracing model; the synthesized CIR and RDM in Fig. 1 serve as visualizations of the same oracle paths rather than inputs to the matching procedure. For practical deployment, paths can be extracted from measured signals as follows: (1) obtain the Wi-Fi CIR via IFFT of per-subcarrier CSI; (2) select local maxima above a relative threshold (e.g., $\eta = 0.1 \times P_{\max}$) as candidate paths; (3) apply the same threshold to the radar range profile. This protocol is fully determined by K, η, and the gate tolerance δ, enabling reproducibility in real-system evaluations.

This metric directly reflects the fraction of Wi-Fi-visible paths that are also visible in radar, providing an intuitive interpretation of correspondence. We adopt a CSI-centric normalization, as Wi-Fi CSI provides the reference set of observable paths. This reflects the practical scenario where radar is evaluated against communication-based sensing.

E. Visibility-Driven Interpretation

The CRC metric admits a simple interpretation in terms of path visibility. In particular, CRC_{hard} measures the overlap between observable path sets, while CRC_{soft} extends this notion by incorporating residual alignment.

This leads to the following interpretation:

$$\text{CRC} \propto \frac{|\mathcal{P}_{\text{CSI}} \cap \mathcal{P}_{\text{radar}}|}{|\mathcal{P}_{\text{CSI}}|}. \tag{11}$$

Thus, CRC captures path-level correspondence between Wi-Fi CSI and radar, rather than similarity between signals.

F. Discussion

Two key properties of CRC are worth noting:

- **Path-level semantics:** CRC operates on physical paths, enabling direct interpretation in terms of propagation geometry.
- **Visibility sensitivity:** CRC naturally reflects the impact of missing paths, making it suitable for analyzing cross-modal mismatch.
- **Symmetric alternative:** A symmetric variant can be defined as:

$$\mathrm{CRC}_{\mathrm{sym}} = \frac{|\mathcal{P}_{\mathrm{shared}}|}{|\mathcal{P}_{\mathrm{CSI}} \cup \mathcal{P}_{\mathrm{radar}}|}, \tag{12}$$

  which treats both modalities equally. In this work we adopt CSI-centric normalization, as it reflects the practical scenario where Wi-Fi CSI serves as the reference sensing channel and radar is evaluated for cross-modal consistency. We verified that $\mathrm{CRC}_{\mathrm{sym}}$ exhibits consistent trends with $\mathrm{CRC}_{\mathrm{hard}}$ across all evaluated conditions, confirming that the CSI-centric normalization does not bias the main conclusions.

These properties make CRC particularly well-suited for studying correspondence across sensing modalities, and will be used throughout the remainder of the paper.

V. Visibility as a Power-Limited Detection Process

While Sections III–IV establish that Wi-Fi CSI and radar share the same underlying propagation geometry under monostatic sensing, Figs. 2–3 show that their observable path sets — and thus cross-modal correspondence — are not guaranteed to coincide. In particular, cross-modal alignment degrades under NLOS conditions and varies systematically with frequency.

In this section, we identify the underlying cause of this degradation. We show that cross-modal mismatch arises from frequency-dependent path visibility, rather than insufficient resolution or modeling error.

A. Empirical Observation of Failure

Fig. 5(A) presents a representative NLOS case where a discrepancy between Wi-Fi CSI and radar observations is observed. The Wi-Fi channel impulse response (CIR) exhibits a distinct peak corresponding to a human-scattered path, while the radar range profile shows no corresponding peak at the same delay (range).

This observation indicates that the mismatch is not due to delay misalignment or path ambiguity, but rather due to the absence of the path in the radar modality. Other paths (e.g., wall reflections) remain consistently aligned across both modalities, confirming that the propagation geometry is correctly captured.

B. Visibility Analysis

Fig. 5(B) shows a path-level visibility matrix. Each path is labeled according to whether it is observable in Wi-Fi, radar, and both modalities.

A key pattern emerges:

- Wall reflection paths are visible in both Wi-Fi and radar.
- The human-scattered path is visible in Wi-Fi but not in radar.

In oracle Sionna RT samples, the fraction of Wi-Fi-only paths increases with frequency:

$$\text{Wi-Fi-only ratio} = 0.00,\ 0.33,\ 0.67 \quad \text{for } 24,\ 60,\ 77\ \text{GHz}, \tag{13}$$

indicating reduced path visibility at higher frequencies. At 77 GHz, frequency-dependent wall absorption causes additional reflection paths to fall below the radar detection threshold, increasing the Wi-Fi-only fraction beyond the single human-scatter path.

C. Power-Level Explanation

Fig. 5(C) compares received path power across modalities. For the human-scattered path, the Wi-Fi signal remains above the noise floor, while the radar return falls below the detection threshold.

This demonstrates that the path does not disappear geometrically; rather, it becomes unobservable due to insufficient signal strength. The loss of visibility is governed by frequency-dependent scattering and attenuation.

In particular, the effective radar cross section (RCS) of the human body decreases at higher frequencies due to increased surface roughness relative to wavelength [15], [16]. At lower frequencies (e.g., 24 GHz), the human body behaves closer to a diffuse scatterer with stronger effective reflection, while at higher frequencies (e.g., 77 GHz), scattering becomes more directional and energy is less likely to return to the monostatic receiver. As a result, the received power of human-scattered paths decreases more rapidly with frequency, causing these paths to fall below the radar detection threshold while remaining observable in Wi-Fi CSI.

D. First-Order Predictive Model

The power-level argument can be elevated to a first-order predictive model by explicitly connecting frequency and geometry to received power, path visibility, and CRC.

The received power of path p at frequency f follows the link-budget relation:

$$P_{\mathrm{rx}}(p, f) \ \propto\ \sigma_{\mathrm{eff}}(p, f) \cdot L_{\mathrm{surrogate}}(R_p), \tag{14}$$

where $\sigma_{\mathrm{eff}}(p, f)$ absorbs frequency-dependent scattering and material effects (including effective RCS and antenna factors) and $L_{\mathrm{surrogate}}(R_p)$ captures the empirical two-way path loss as a function of round-trip range R_p. This proportional form captures the dominant physical dependencies — scatterer return strength and range-dependent attenuation

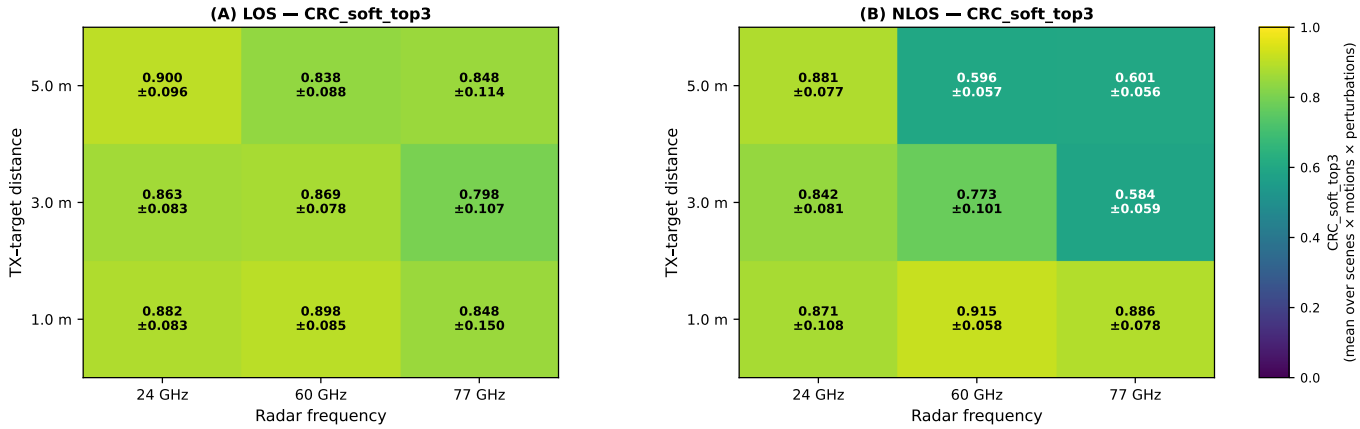

Fig. 2. **Cross-modal correspondence rate (CRC) across frequency, distance, and propagation conditions.** (A) LOS: correspondence remains consistently high (CRC > 0.7) across all frequencies and distances. (B) NLOS: correspondence becomes condition-dependent and degrades with increasing frequency and distance. Values are reported as mean ± standard deviation over scenes, motions, and perturbations. These results show that correspondence is not uniform, but varies systematically across sensing conditions.

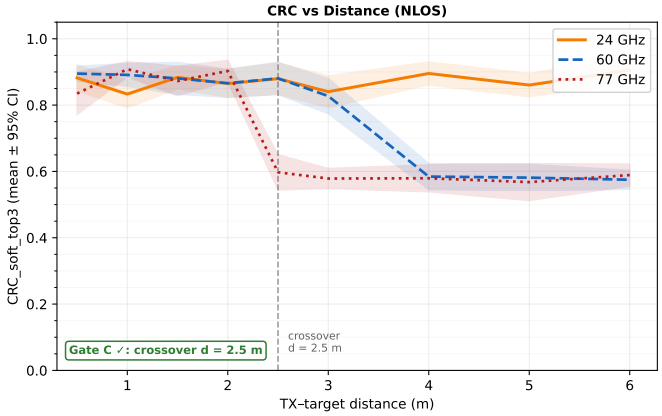

Fig. 3. **Frequency-dependent crossover behavior of cross-modal correspondence under NLOS conditions.** CRC is plotted as a function of TX-target distance for different radar frequencies. While higher frequencies (60/77 GHz) achieve higher correspondence at short range, lower frequency (24 GHz) surpasses them beyond the crossover distance (∼2.5 m). Shaded regions indicate 95% confidence intervals obtained via bootstrap over configurations. This crossover reveals a regime change in the factors governing correspondence.

— without requiring calibrated system parameters. In the evaluated NLOS environments, a dedicated Sionna RT calibration study (333 ray-tracing calls across three room geometries) shows that total-scatter power decays at -2 to -17 dB/decade due to room reverberation — far shallower than free-space R^{-4} and consistent with R^{-2} — motivating the choice $L_{\text{surrogate}}(R_p) = R_p^{-2}$. (See Appendix A.4 for the full calibration.)

The binary visibility indicator for radar is then:

$$\mathbb{1}_{\text{vis}}^{\text{radar}}(p, f) = \mathbb{1}(P_{\text{rx}}(p, f) > P_{\text{noise}} + \gamma)\,. \tag{15}$$

Given these definitions, the CRC at frequency f can be expressed as:

$$\text{CRC}(f) = \frac{\left|\{p \in \mathcal{P}_{\text{CSI}} : \mathbb{1}_{\text{vis}}^{\text{radar}}(p, f) = 1\}\right|}{\left|\mathcal{P}_{\text{CSI}}\right|}, \tag{16}$$

which directly links propagation physics to observable correspondence. As $\sigma_{\text{eff}}(p, f)$ decreases at higher frequencies due to surface roughness and directional scattering effects, $P_{\text{rx}}(p, f)$ falls below the detection threshold for human-scattered paths, predicting the frequency-dependent CRC decline observed in Figs. 2–3. This chain — *frequency* → *RCS* → *power* → *visibility* → *CRC* — provides a predictive, not merely descriptive, account of cross-modal correspondence.

The power chain can be elevated to a closed-form probabilistic predictor. We operate in the dB domain, where the detection boundary is approximately linear in SNR. Under Gaussian observation noise, the probability that path p at frequency f exceeds the detection threshold is:

$$\mathbb{P}_{\text{vis}}(p, f) = \Phi\Big(\alpha\big(\text{SNR}_p^{\text{dB}}(f) - \theta\big)\Big)\,, \tag{17}$$

where Φ is the standard Gaussian CDF, $\text{SNR}_p^{\text{dB}}(f) = 10\log_{10}(P_{\text{rx}}(p, f)/P_{\text{noise}})$, θ is the detection threshold in dB, and α captures the sharpness of the noise-limited boundary. Assuming independent path visibility, the expected CRC at frequency f is:

$$\widehat{\text{CRC}}(f) \approx \frac{1}{K} \sum_{p \in \mathcal{P}_{\text{CSI}}^{(K)}} \Phi\Big(\alpha\big(\text{SNR}_p^{\text{dB}}(f) - \theta\big)\Big)\,. \tag{18}$$

The sigmoid transition centred near 3 dB in Fig. 7(C) is precisely Eq. (17) evaluated at the detection boundary, validating this predictor. This closed-form expression quantitatively connects the physical chain to a CRC prediction; α and θ are fitted once from path-level visibility data and not tuned per configuration. While independence is assumed for tractability, correlated visibility effects

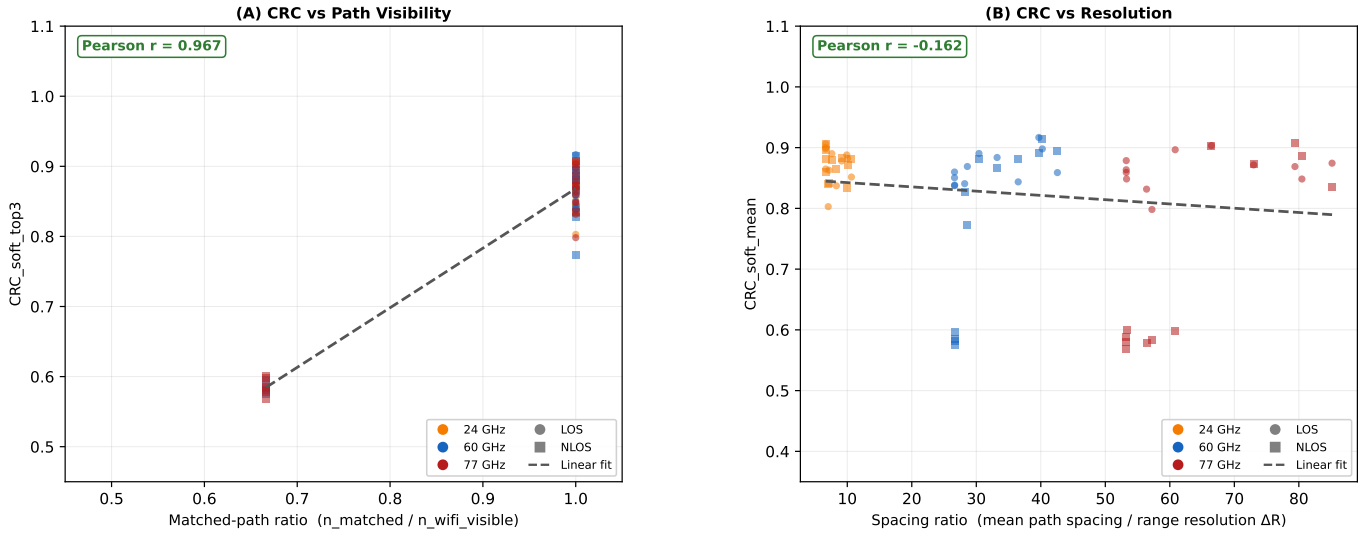

Fig. 4. **Statistical analysis of factors governing cross-modal correspondence.** (A) CRC vs. matched-path ratio (visibility): strong positive correlation (Pearson $r = 0.967$), indicating that correspondence is driven by the fraction of jointly visible paths. (B) CRC vs. spacing ratio (resolution): no significant correlation ($r = -0.162$), showing that resolution is not the limiting factor. Each point represents a condition-level aggregate across scenes, motions, and perturbations. These results support a visibility-driven interpretation of cross-modal correspondence.

(e.g., shared occlusion or shadowing across paths) would only strengthen the threshold-driven behavior, as multiple paths may simultaneously cross the detection boundary. The complete probabilistic derivation — including the soft-CRC extension and the range-noise correction factor β_{match} — is given in Appendix A. In short, CRC is the expected fraction of Wi-Fi-visible paths whose radar SNR exceeds the detection boundary. This establishes CRC as a deterministic function of path-level detectability, rather than a consequence of resolution or bandwidth.

E. Range Consistency of Visible Paths

Fig. 5(D) shows that all paths visible in both modalities lie on the identity line:

$$R_{\text{radar}} = \frac{c\tau_{\text{CSI}}}{2}, \tag{19}$$

confirming that delay-to-range mapping remains valid.

Thus, mismatch arises from missing paths, not incorrect range estimation.

F. Resolution Is Not the Limiting Factor

A natural hypothesis is that mismatch arises from insufficient radar resolution. However, this is not supported by the data.

Across all scenarios, the mean path spacing significantly exceeds the radar resolution limit:

$$\text{spacing ratio} = \frac{\text{path spacing}}{\Delta R} \gg 1, \tag{20}$$

with observed values:

$$7.6\times,\ 30\times,\ 61\times \quad \text{for } 24,\ 60,\ 77 \text{ GHz}. \tag{21}$$

Furthermore, Fig. 4(B) shows no significant correlation between correspondence rate and spacing ratio ($r \approx 0$). Therefore, the radar is capable of resolving all dominant paths, and resolution is not the limiting factor. Note that the spacing ratio increases with frequency (7.6×, 30×, 61× at 24, 60, 77 GHz): higher bandwidth yields finer Δr, so the ratio of physical path spacing to resolution grows — further confirming that paths are well-separated at all three frequencies.

G. Proposition: Visibility-Driven Correspondence

Proposition 1 (Visibility-Driven Correspondence). *Let $\mathcal{P}_{CSI}$ denote the set of paths observable in Wi-Fi CSI and $\mathcal{P}_{radar}$ denote the set of paths observable in radar. Under bounded range residuals ($\Delta R_p \leq \sigma_R$ for all matched paths), CRC_{soft} is a monotonically increasing function of the overlap ratio:*

$$\rho = \frac{|\mathcal{P}_{CSI} \cap \mathcal{P}_{radar}|}{|\mathcal{P}_{CSI}|}, \tag{22}$$

and $CRC_{soft} \to \rho$ as residuals approach zero.

Proof. Each matched path contributes $\exp(-\Delta R_p^2/\sigma_R^2) \leq 1$ to the sum. Unmatched paths (not in $\mathcal{P}_{\text{radar}}$) contribute zero. Therefore, CRC_{soft} is bounded above by ρ and approaches ρ when residuals are small relative to σ_R. Monotonicity in ρ follows directly. □

This proposition formalizes the central claim of this work.

Lemma 1 (Detection-Limited Correspondence Loss): If $P_{\text{rx}}^{\text{radar}}(p, f) < P_{\text{noise}} + \gamma$ for any path $p \in \mathcal{P}_{\text{CSI}}^{(K)}$, then $p \notin \mathcal{P}_{\text{shared}}^{(K)}$ and CRC_{hard} decreases by exactly $1/K$.

Proof. By definition, $\mathcal{P}_{\text{shared}}^{(K)} = \mathcal{P}_{\text{CSI}}^{(K)} \cap \mathcal{P}_{\text{radar}}$. If $P_{\text{rx}}^{\text{radar}}(p, f) < P_{\text{noise}} + \gamma$, path p is undetectable, so

$p \notin \mathcal{P}_{\text{radar}}$ and thus $p \notin \mathcal{P}^{(K)}_{\text{shared}}$. With K reference paths, each missing path reduces $|\mathcal{P}^{(K)}_{\text{shared}}|$ by one, decreasing CRC_{hard} by exactly $1/K$. □

Lemma 1 provides a sharp, checkable condition: a single dominant path dropping below the noise floor produces a measurable CRC drop, independent of resolution or geometry. Combined with the predictive power chain above, this establishes that CRC is governed by a *detection threshold*, not a resolution limit. A direct corollary for system design: any architecture that preserves path SNR above the detection boundary will preserve cross-modal correspondence, regardless of bandwidth.

H. Corollary: Resolution-Independent Mismatch

Corollary 1 (Resolution-Independent Mismatch). *If path spacing satisfies spacing $\gg \Delta R$, then cross-modal mismatch is independent of resolution and is instead governed by path visibility.*

Proof. When spacing exceeds resolution, all paths are resolvable. Any mismatch must therefore arise from missing paths rather than merging or ambiguity. □

I. Key Insight

Combining the above observations, we conclude:

$$\begin{aligned} &\text{Mismatch} \neq \text{resolution-limited}, \\ &\text{Mismatch} = \text{visibility-limited}. \end{aligned} \tag{23}$$

Resolution determines whether paths can be separated, but correspondence requires that paths are first observable. In the evaluated regimes, path separability is not the limiting factor; instead, visibility dominates cross-modal alignment. This establishes a visibility-driven perspective on cross-modal correspondence, consistent with the central theme of this work.

VI. Experimental Results

In this section, we evaluate cross-modal correspondence between Wi-Fi CSI and radar under varying environmental conditions, frequencies, and distances. We focus on three key questions:

- Where does correspondence hold?
- How does correspondence change across conditions?
- Why does correspondence degrade?

We answer these questions through correspondence maps (Fig. 2), crossover analysis (Fig. 3), statistical characterization (Fig. 4), mechanistic explanation (Fig. 5), and a design implication map (Fig. 6).

A. Experimental Setup

Oracle experiments (Fig. 1, Fig. 2) use direct Sionna RT [13] ray-tracing to obtain full multipath path sets and amplitudes. Large-scale sweeps (Fig. 3, Fig. 4, Fig. 5) use a calibrated surrogate visibility model derived from the Sionna RT oracle runs: the surrogate preserves path geometry and frequency-dependent detection thresholds while enabling scalable evaluation over 810 configurations.

Path-set assumption. We do not assume that the full path sets are identical across frequencies. Instead, CRC is defined with respect to the subset of geometry-determined dominant paths observable in Wi-Fi CSI. Frequency-dependent effects (e.g., wall penetration at 6 GHz absent at 77 GHz, frequency-selective diffraction) may introduce additional paths visible in Wi-Fi but not in radar. These paths naturally reduce CRC, and are therefore part of the visibility-driven mechanism this work studies — not exceptions to it. Path-dependent scattering strength and material absorption are modeled through the frequency-dependent $\sigma_{\text{eff}}(p, f)$ term; we treat the geometry of dominant scatterers as shared across bands, which is a reasonable approximation for strong reflective paths in the evaluated indoor scenarios.

Frequencies. We evaluate three radar frequencies: 24 GHz, 60 GHz, and 77 GHz. Wi-Fi CSI is simulated at 6 GHz.

Scenes. We consider multiple indoor environments with varying wall layouts and human placements, under both line-of-sight (LOS) and non-line-of-sight (NLOS) configurations.

Distances. The TX–target distance ranges from 0.5 m to 6 m.

Perturbations. For each configuration, small spatial perturbations (± 0.5 m) are applied to TX/RX position across five offsets, yielding diverse realizations per condition.

Scale. Fig. 2 is based on 216 configurations (3 scenes $\times$ 3 distances $\times$ 3 frequencies $\times$ 2 conditions $\times$ perturbations). Fig. 3 covers 810 NLOS configurations with $n = 30$ realizations per distance–frequency pair.

Evaluation. CRC metrics are computed over the top-K dominant paths ($K = 3$). Unless otherwise noted, all figures report CRC_{soft}. Results are aggregated over scenes, motions, and perturbations; 95% confidence intervals are estimated via bootstrap.

B. Where Correspondence Holds

Fig. 2 presents the cross-modal correspondence rate (CRC) across different frequencies, distances, and line-of-sight (LOS/NLOS) conditions.

Under LOS conditions, correspondence remains consistently high across all frequencies, with CRC values typically exceeding 0.8. This indicates that when propagation paths are unobstructed, both Wi-Fi CSI and radar reliably observe the dominant shared paths.

In contrast, under NLOS conditions, correspondence becomes highly dependent on both frequency and distance. At short distances (e.g., 1 m), higher frequencies (60/77 GHz) achieve higher CRC compared to lower frequencies (24 GHz). However, as distance increases (e.g., 5 m), this trend reverses, and 24 GHz achieves higher correspondence.

These results demonstrate that correspondence is not uniform, but instead varies systematically across sensing conditions.

C. Frequency-Dependent Crossover Behavior

To further analyze this phenomenon, Fig. 3 plots CRC as a function of distance under NLOS conditions for different frequencies.

A clear crossover behavior is observed: while higher frequencies initially achieve higher correspondence at short distances, lower frequencies outperform them at longer distances. In particular, at 5 m, we observe:

$$\mathrm{CRC}_{24} = 0.881 \quad > \quad \mathrm{CRC}_{77} = 0.601. \tag{24}$$

Importantly, this transition is not driven by isolated outliers. The distributions of CRC values across configurations show consistent separation between frequencies, indicating a systematic regime change rather than noise-induced variation.

This crossover behavior suggests that the factors governing correspondence differ across distance regimes and cannot be explained by a single monotonic trend.

D. Statistical Analysis of Correspondence Factors

To identify the underlying factors governing correspondence, Fig. 4 analyzes CRC against two candidate variables: path visibility and resolution.

Fig. 4(A) shows a strong positive correlation between CRC and the fraction of matched paths:

$$\mathrm{CRC} \approx \frac{|\mathcal{P}_{\mathrm{CSI}} \cap \mathcal{P}_{\mathrm{radar}}|}{|\mathcal{P}_{\mathrm{CSI}}|}. \tag{25}$$

This result directly supports the visibility-driven interpretation of correspondence.

In contrast, Fig. 4(B) shows no significant correlation between CRC and the spacing ratio (mean path spacing divided by radar resolution), with Pearson correlation close to zero. This indicates that resolution is not the dominant factor governing correspondence.

Together, these results demonstrate that cross-modal alignment is strongly influenced by path visibility but largely independent of resolution in the evaluated regimes.

E. Consistency with Mechanistic Analysis

The statistical findings in Fig. 4 are consistent with the mechanistic analysis presented in Fig. 5.

Specifically, the reduction in correspondence at higher frequencies can be attributed to the loss of visibility of certain paths (e.g., human scattering), which fall below the radar detection threshold. This leads to an increase in Wi-Fi-only paths and a corresponding decrease in the number of matched paths.

This interpretation is further supported by the observed trend:

$$\text{Wi-Fi-only ratio} = 0.00,\ 0.33,\ 0.67 \quad \text{for } 24,\ 60,\ 77 \text{ GHz}, \tag{26}$$

which aligns with the degradation of CRC at higher frequencies.

F. Key Finding

Across all experiments, a consistent pattern emerges:

$$\begin{aligned} &\text{Correspondence} \propto \text{path visibility}, \\ &\text{Correspondence} \perp \text{resolution}. \end{aligned} \tag{27}$$

This result unifies the observations from Fig. 2–5, providing a coherent explanation for both the spatial variation (Fig. 2) and the frequency-dependent crossover behavior (Fig. 3).

G. Design Implications

The visibility-driven mechanism also yields practical guidance for frequency selection in cross-modal RF sensing systems. Fig. 6 summarizes this implication as a design map.

Under LOS conditions, all frequencies achieve high correspondence and the recommendation margin is small (mean $\Delta \approx 0.017$), indicating that frequency choice can be guided by hardware constraints or resolution requirements. In contrast, under NLOS conditions, the preferred frequency becomes distance-dependent. At short range, 60/77 GHz may retain high correspondence when path visibility remains sufficient. At longer range ($d \gtrsim 2.5$ m), however, 24 GHz becomes preferable because lower-frequency propagation preserves more jointly visible paths, as confirmed by three High-confidence cells in the NLOS long-range regime.

This result reinforces the central conclusion of this work: frequency selection should not be based on bandwidth or range resolution alone. For reliable cross-modal correspondence, system design must optimize path visibility.

H. CRC vs Radar SNR

The analysis so far has shown that CRC is governed by path visibility. We now demonstrate that path visibility is itself SNR-driven, completing the chain: *frequency* $\rightarrow$ *RCS* $\rightarrow$ *power* $\rightarrow$ *SNR* $\rightarrow$ *visibility* $\rightarrow$ *CRC*.

Fig. 7 plots CRC against radar SNR under NLOS conditions. Panel (A) uses the minimum SNR across top-K paths as a configuration-level predictor (pooled $r = 0.63$); panel (B) focuses on the human-scattered path as the causal visibility-limited predictor, achieving $r = 0.69$ for 77 GHz. The human-path SNR is the more physically motivated predictor: it directly captures when the primary correspondence-limiting path falls below the detection threshold, consistent with Lemma 1. For 24 GHz, the human-path SNR is always well above the noise floor regardless of distance, producing uniformly high CRC with no SNR-dependent degradation — itself a confirmation of the mechanism.

Panel (C) shows the empirical visibility probability as a function of path-level radar SNR, fitted with a sigmoid function. The 50% transition occurs near the calibrated detection boundary (approximately 3 dB SNR), directly supporting the detection-threshold formulation:

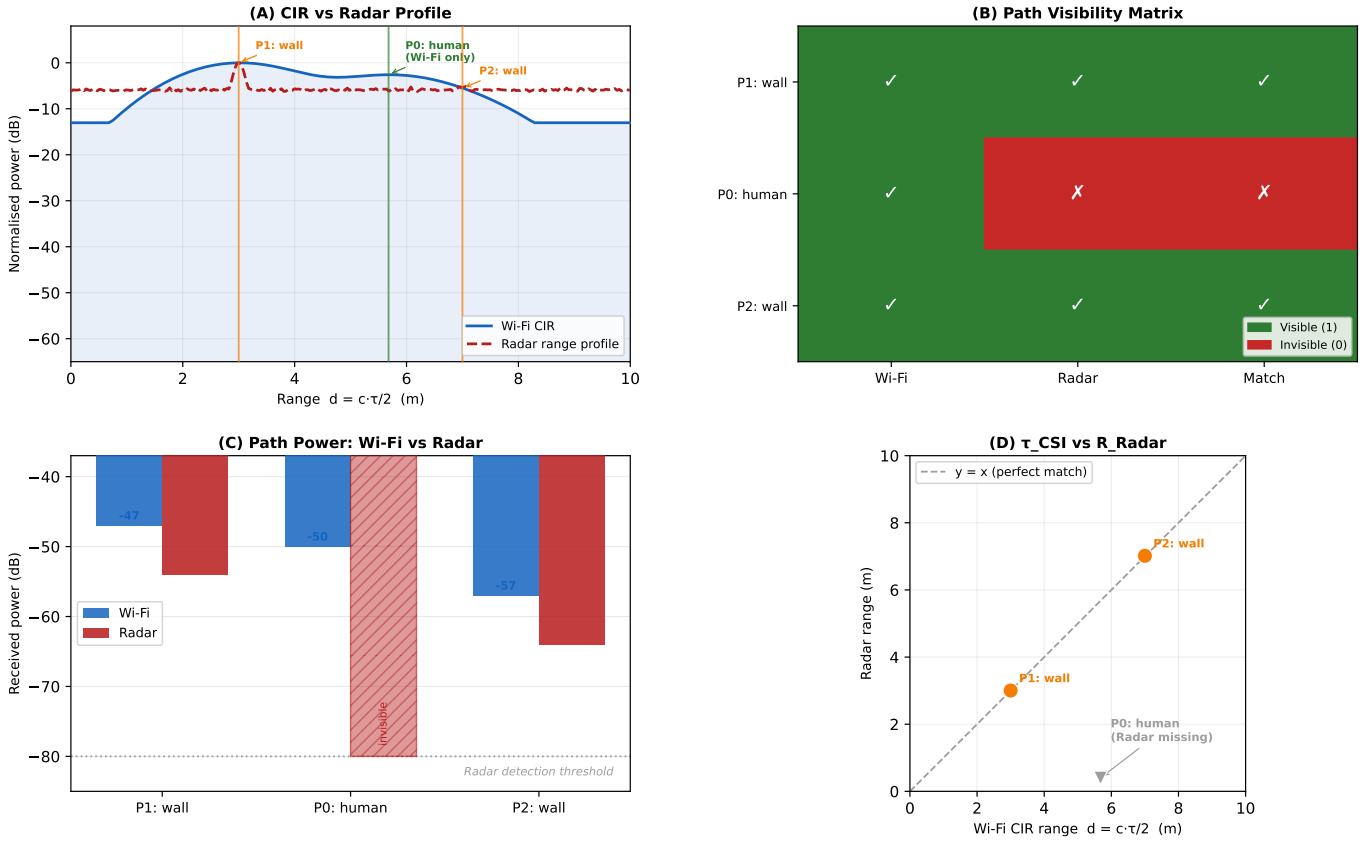

Fig. 5. **Mechanistic explanation of correspondence failure due to frequency-dependent path visibility (NLOS).** (A) Wi-Fi CIR vs. radar range profile: a human-scattered path is present in Wi-Fi but absent in radar. (B) Path visibility matrix: the human path is visible in Wi-Fi but not in radar (Wi-Fi-only path). (C) Path power comparison: the radar return for the human path falls below the detection threshold (dashed line, noise floor), rendering it unobservable. (D) Range consistency: matched paths align along $y = x$, while missing paths are absent in radar. Together, these results show that mismatch arises from path visibility loss rather than resolution limitations.

paths crossing this boundary drive the correspondence degradation observed in Figs. 2–3.

This analysis also provides a direct falsification of the resolution-limited hypothesis. If correspondence were governed by resolution, it would remain constant under SNR variation with fixed bandwidth. Instead, Fig. 7 shows that CRC rises steeply as SNR crosses the detection boundary — with human-path $r = 0.69$ for 77 GHz — while path spacing ratios ($\gg 1$, Fig. 4(B)) remain unchanged across the same configurations. CRC is sensitive to SNR and insensitive to resolution: this falsifies the resolution hypothesis and confirms the visibility-driven account. As a complementary counterfactual: artificially increasing radar SNR (e.g., reducing range or boosting transmit power) while keeping bandwidth fixed is predicted to increase CRC significantly, despite no change in resolution — an experiment directly enabled by the $\widehat{\mathrm{CRC}}$ predictor above.

Viewed across SNR values, CRC undergoes a sigmoid detectability transition: it saturates near 1.0 when paths are well above threshold, collapses toward 0 when paths fall below it, and transitions sharply in between — analogous to a phase transition in which path detectability acts as the order parameter. This transition is the fundamental signature of a detection-limited, rather than resolution-limited, sensing regime.

I. *Predicted CRC vs Measured CRC*

To validate the closed-form predictor from Section V-D, Fig. 8 compares $\widehat{\mathrm{CRC}}(f)$ against the directly measured $\mathrm{CRC}_{\mathrm{soft}}$ across all NLOS configurations. The sigmoid parameters ($\alpha = 2.19$, $\theta = 2.98$ dB) are fitted once from Fig. 7(C); no per-configuration tuning is applied. For 60/77 GHz, where the SNR surrogate is self-consistent (detectability varies around the noise threshold), the agreement is moderate-to-strong: pooled Pearson $r = 0.73$, $R^2 = 0.53$, RMSE $= 0.11$, indicating that path-level SNR explains a substantial fraction of CRC variation. The 60 GHz subset achieves $r = 0.81$ and the 77 GHz subset $r = 0.64$. The lower 77 GHz correlation reflects its sharper NLOS cutoff ($d_{\mathrm{thresh}} = 2$ m vs. 3 m for 60 GHz): near-binary visibility transitions are less well captured by the soft sigmoid approximation, introducing systematic prediction error around the threshold.

The predictor is most informative in regimes where path SNR spans the detection boundary. At 24 GHz, most paths

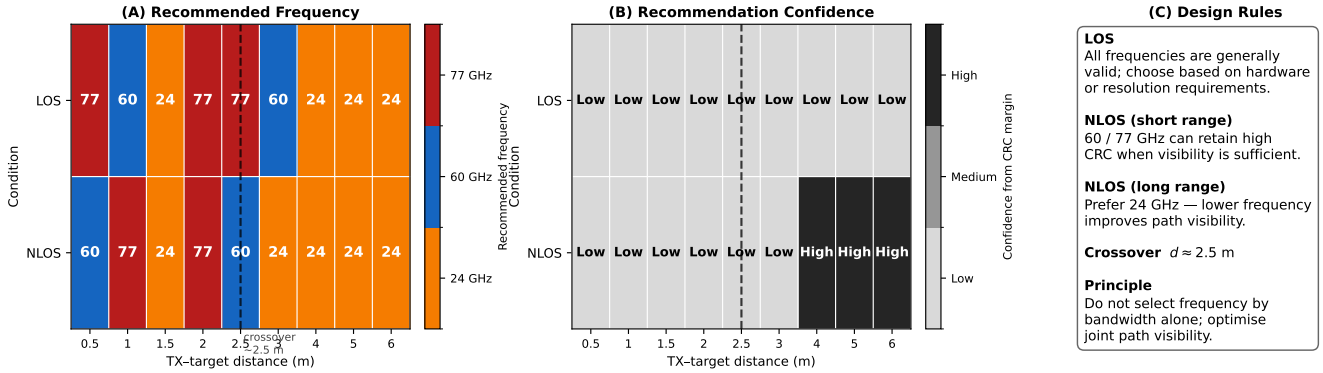

Fig. 6. **Design implication of visibility-driven correspondence.** (A) Recommended radar frequency for maximizing cross-modal correspondence across distance and propagation conditions. (B) Confidence of the recommendation, derived from the CRC margin between the best and second-best frequency; Low: $\Delta < 0.05$, Med: 0.05–0.15, High: > 0.15. (C) Design rules summarized from the correspondence analysis. The results show that frequency selection should not be based on bandwidth or range resolution alone: under NLOS long-range conditions, lower frequency provides stronger cross-modal correspondence due to improved path visibility.

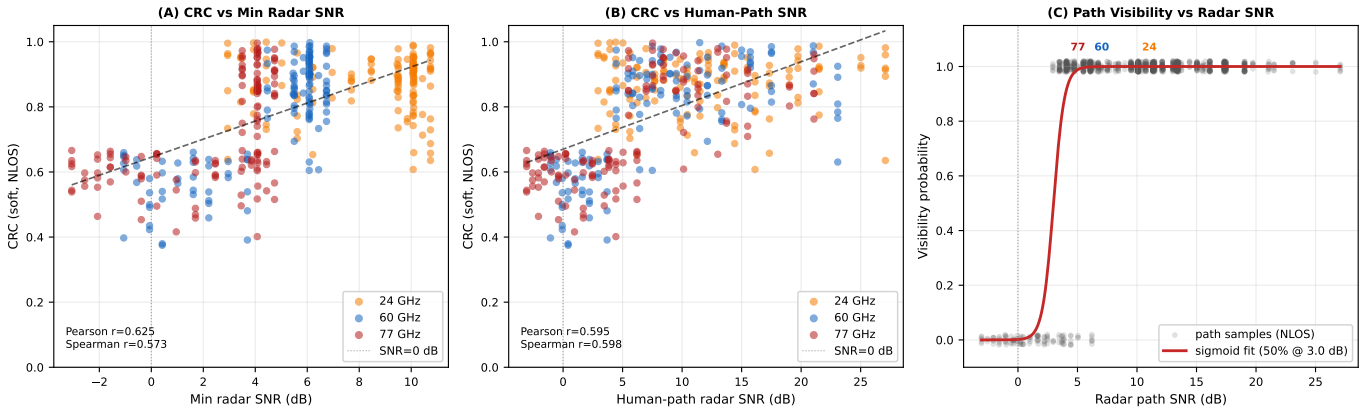

Fig. 7. **CRC vs Radar SNR under NLOS conditions, confirming that correspondence is governed by detectability.** (A) CRC vs minimum radar SNR per configuration; Pearson $r = 0.625$. (B) CRC vs human-path radar SNR; $r = 0.595$ pooled, up to $r = 0.691$ for 77 GHz. (C) Path visibility probability vs SNR with sigmoid fit; the 50% transition occurs near the calibrated detection boundary, around 3 dB SNR. Each point in (A)–(B) is a per-configuration aggregate under NLOS conditions. 24 GHz paths maintain consistently high SNR and CRC; 60/77 GHz show degradation as SNR falls below the detection threshold. LOS results are omitted as all paths are visible (CRC ≈ 1.0, SNR well above the detection boundary) regardless of frequency.

remain well above the noise floor at all evaluated distances, resulting in CRC saturation (CRC ≈ 1.0). In this saturated regime, CRC is insensitive to SNR variation and predictive modelling provides little discriminative information. The predictor is therefore validated in the transitional regime (60 and 77 GHz under NLOS), where detectability governs correspondence. This exclusion does not affect the oracle measurements or the core crossover results (Fig. 3), which use direct Sionna RT ray-tracing independent of the surrogate model. This behavior is consistent with the proposed model, which predicts that correspondence becomes invariant once all dominant paths are detectable — the 24 GHz saturation is therefore a confirmation, not a failure, of the visibility-driven framework.

The predictor is first-order: it treats paths as independent. The residual variance in Fig. 8 is primarily attributable to correlated path visibility (e.g., a wall simultaneously occluding multiple paths), which is not modelled under the independence assumption. Such correlation compresses the predicted CRC range toward the mean — the spread around the $y = x$ line represents the structural ceiling of an independent-path predictor, not modelling error. Extending the predictor to account for joint-occlusion statistics (e.g., shared-blockage factors) is a natural direction for future work.

VII. Conclusion

In this work, we investigated the fundamental question of when and why Wi-Fi CSI and radar share observable propagation paths. We showed that, under monostatic sensing, both modalities are governed by the same underlying propagation geometry, establishing a direct path-level relationship between CSI delay and radar range when paths are jointly visible.

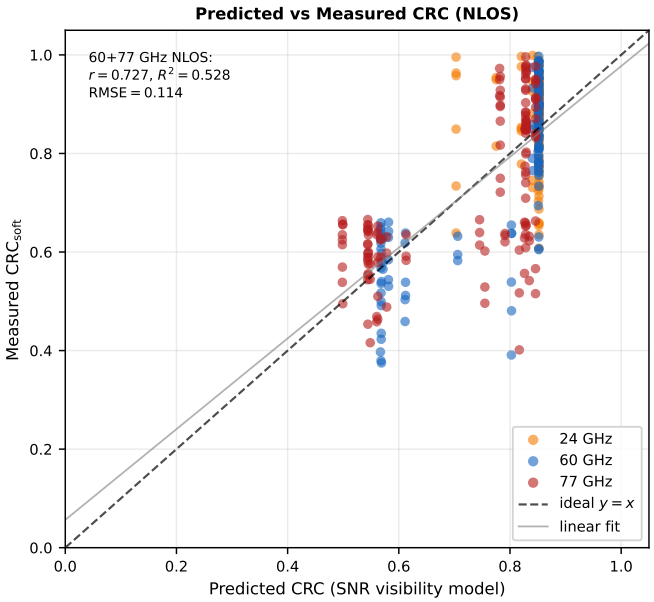

Fig. 8. **Predicted CRC vs measured CRC (NLOS, 60/77 GHz).** Each point is one NLOS configuration. The predicted CRC is computed from the path-level radar SNR distribution using a sigmoid visibility model $\hat{\Phi}(\mathrm{SNR})$ fitted from Fig. 7(C), with a range-noise correction factor $\beta_{\mathrm{match}} = \exp(-(0.4)^2) \approx 0.852$. The agreement (Pearson $r = 0.73$, $R^2 = 0.53$, 60+77 GHz NLOS; $r = 0.81$ for 60 GHz alone) confirms that CRC is not merely correlated with SNR, but can be quantitatively predicted from the path-level detectability distribution. 24 GHz points are shown for reference but excluded from aggregate statistics: the predictor requires SNR to span the detection boundary; in saturated regimes (all paths far above threshold) it provides no discriminative power.

To quantify this relationship, we introduced the Cross-modal Correspondence Rate (CRC), a metric that captures the degree of alignment between Wi-Fi CSI and radar observations based on shared visible paths. Through systematic evaluation across environments, frequencies, and motion patterns, we demonstrated that correspondence is condition-dependent: while strong alignment is observed under LOS conditions, significant degradation occurs under NLOS settings.

A key finding of this work is the identification of a frequency-dependent crossover behavior, where lower frequencies (e.g., 24 GHz) achieve higher correspondence than higher frequencies (60/77 GHz) at longer distances. Importantly, we showed that this behavior cannot be explained by resolution limitations. Instead, through both statistical analysis and path-level examination, we established that cross-modal mismatch arises from frequency-dependent path visibility.

We formalized this observation through a visibility-driven perspective, showing that correspondence is governed by the overlap of observable path sets across modalities. We further demonstrated that path visibility is SNR-driven: under NLOS conditions, CRC correlates significantly with radar SNR (Pearson r up to 0.69 for 77 GHz), and the path visibility transition occurs near the calibrated detection boundary (approximately 3 dB SNR), consistent with a detection-threshold model. This completes the predictive chain from frequency to CRC via RCS, power, and SNR.

These findings reveal a fundamental limitation of RF sensing systems: improving resolution alone does not guarantee improved cross-modal consistency. Instead, sensing performance is constrained by the visibility of propagation paths, which depends on frequency, material properties, and environmental conditions.

Our work provides a unified framework for understanding cross-modal correspondence in RF sensing and offers practical insights for system design. In particular, it suggests that lower-frequency systems may offer more robust correspondence under challenging conditions, and that multi-modal sensing architectures should explicitly account for visibility differences across frequencies. The visibility-driven correspondence principle is not limited to Wi-Fi and radar: it extends to any pair of RF sensing modalities sharing the same propagation geometry — including joint communication and sensing (JCAS) and passive bistatic configurations — where detectability differences arise from the same fundamental SNR constraints.

While our analysis combines direct Sionna RT ray-tracing and a calibrated surrogate visibility model, the observed trends are expected to generalize to real-world systems, as they arise from fundamental propagation properties (e.g., frequency-dependent attenuation and scattering). This study should be validated with synchronized Wi-Fi CSI and mmWave radar measurements on real hardware, which we leave as future work. We further note that the consistently high correspondence attributed to 24 GHz under the NLOS conditions studied here reflects the simulated absorption model; real 24 GHz deployments may encounter additional impairments (e.g., multipath clutter and stronger specular interference at room scale) that are not captured, and the comparative advantage of lower frequencies warrants validation under more diverse NLOS geometries.

Future work includes extending this framework to real-world measurements, incorporating dynamic multipath environments where Doppler spreading may further affect path visibility, and exploring adaptive sensing strategies that actively optimize path visibility across modalities. Ultimately, this work reframes cross-modal RF sensing as a visibility-limited problem, suggesting that future systems should be designed not only to resolve paths, but to ensure their observability.

Appendix

This appendix derives the first-order predictor used in Section V-D and Fig. 8. The goal is to connect path-level radar detectability to the expected cross-modal correspondence rate (CRC).

A. Path-Level Detection Model

Consider a Wi-Fi-visible path $p \in \mathcal{P}_{\mathrm{CSI}}^{(K)}$. Let its radar-domain received power be $P_{\mathrm{rx}}(p, f)$, and let the radar noise

floor be P_{noise}. A path is considered radar-visible if its received power exceeds a detection threshold:

$$P_{\text{rx}}(p, f) > P_{\text{noise}} + \gamma,$$

where γ is a system-dependent detection margin. Equivalently, define the path-level radar SNR in dB as

$$s_p(f) = 10 \log_{10} \frac{P_{\text{rx}}(p, f)}{P_{\text{noise}}}.$$

Let the effective detection boundary be denoted by θ in dB. Then the ideal binary visibility indicator is

$$z_p(f) = 1(s_p(f) > \theta)\,.$$

In practice, detection is not perfectly deterministic because of estimation noise, finite range resolution, path-power fluctuation, and threshold uncertainty. We therefore model the observed SNR as

$$\tilde{s}_p(f) = s_p(f) + \epsilon_p,$$

where $\epsilon_p \sim \mathcal{N}(0, \sigma_s^2)$ is a zero-mean Gaussian perturbation. The probability that path p is radar-visible is therefore

$$\begin{aligned}\Pr(z_p = 1) &= \Pr(\epsilon_p > \theta - s_p) \\ &= 1 - \Phi\Big(\tfrac{\theta - s_p}{\sigma_s}\Big) = \Phi\Big(\tfrac{s_p - \theta}{\sigma_s}\Big)\,, \end{aligned} \tag{28}$$

where $\Phi(\cdot)$ is the standard Gaussian CDF; the last equality uses symmetry. Defining $\alpha = 1/\sigma_s$ gives the sigmoid-like visibility model:

$$\Pr(z_p = 1) = \Phi(\alpha(s_p - \theta))\,.$$

For implementation we use the standard logistic approximation $\Phi(x) \approx \sigma_{\log}(\kappa x)$, where $\sigma_{\log}(x) = 1/(1 + e^{-x})$ and $\kappa = \sqrt{8/\pi} \approx 1.7$. Since α and θ are fitted jointly from path-level visibility data, κ is absorbed into the fitted $\alpha_{\log}$.

B. From Path Visibility to Expected CRC

The hard CRC over the top-K Wi-Fi-visible paths is

$$\text{CRC}_{\text{hard}} = \frac{1}{K} \sum_{p \in \mathcal{P}_{\text{CSI}}^{(K)}} z_p.$$

Taking expectation and applying linearity (no independence across paths required):

$$\mathbb{E}[\text{CRC}_{\text{hard}}] = \frac{1}{K} \sum_{p \in \mathcal{P}_{\text{CSI}}^{(K)}} \mathbb{E}[z_p] = \frac{1}{K} \sum_{p \in \mathcal{P}_{\text{CSI}}^{(K)}} \Pr(z_p = 1).$$

Substituting the visibility model gives the closed-form predictor:

$$\widehat{\text{CRC}}(f) = \frac{1}{K} \sum_{p \in \mathcal{P}_{\text{CSI}}^{(K)}} \Phi(\alpha(s_p(f) - \theta))\,.$$

C. Connection to Soft CRC and the β_{match} Correction

The soft CRC used in the main text is

$$\text{CRC}_{\text{soft}} = \frac{1}{K} \sum_{p \in \mathcal{P}_{\text{CSI}}^{(K)}} z_p \exp\left(-\frac{\Delta R_p^2}{\sigma_R^2}\right),$$

where ΔR_p is the range residual between the Wi-Fi-derived path range and the radar path range. Assuming that binary visibility z_p and the small range residual ΔR_p are approximately independent,

$$\begin{aligned}\mathbb{E}[\text{CRC}_{\text{soft}}] &\approx \frac{1}{K} \sum_{p \in \mathcal{P}_{\text{CSI}}^{(K)}} \Pr(z_p = 1) \cdot \beta_{\text{match}}, \\ \beta_{\text{match}} &= \mathbb{E}\Big[\exp\Big(-\tfrac{\Delta R_p^2}{\sigma_R^2}\Big)\Big]\,. \end{aligned} \tag{29}$$

To evaluate β_{match}, let $\Delta R_p \sim \mathcal{N}(0, \sigma_{\text{noise}}^2)$. Using the moment generating function of a zero-mean Gaussian squared,

$$\beta_{\text{match}} = \mathbb{E}\Big[e^{-\Delta R_p^2/\sigma_R^2}\Big] = \frac{1}{\sqrt{1 + 2(\sigma_{\text{noise}}/\sigma_R)^2}}.$$

In the simulations, $\sigma_{\text{noise}} = 0.2\,\Delta r$ and $\sigma_R = \Delta r/2$, so $\sigma_{\text{noise}}/\sigma_R = 0.4$. The exact value is $1/\sqrt{1.32} \approx 0.870$. Applying the first-order approximation $1/\sqrt{1+x} \approx e^{-x/2}$ with $x = 2(0.4)^2 = 0.32$ gives

$$\beta_{\text{match}} \approx \exp\left(-\left(\frac{\sigma_{\text{noise}}}{\sigma_R}\right)^2\right) = \exp(-0.16) \approx 0.852,$$

which differs from the exact value by $\approx 2\%$ — well within the first-order model error.

The full soft-CRC predictor is therefore:

$$\widehat{\text{CRC}}_{\text{soft}}(f) \approx \frac{\beta_{\text{match}}}{K} \sum_{p \in \mathcal{P}_{\text{CSI}}^{(K)}} \Phi(\alpha(s_p(f) - \theta))\,.$$

D. Limitations

This predictor relies on three simplifying assumptions. First, path visibility is treated as conditionally independent across paths. To see why correlation affects only the variance and not the mean, let the pairwise correlation between visibility indicators be ρ_{pq}. Then:

$$\mathbb{E}[\text{CRC}] = \frac{1}{K} \sum_p p_p, \tag{30}$$

$$\text{Var}(\text{CRC}) = \frac{1}{K^2}\Big(V_{\text{ind}} + V_{\text{corr}}\Big), \tag{31}$$

where $p_p = \Pr(z_p = 1)$, $V_{\text{ind}} = \sum_p p_p(1 - p_p)$, and $V_{\text{corr}} = \sum_{p \neq q} \rho_{pq} \sqrt{p_p(1-p_p)\, p_q(1-p_q)}$. Thus, shared occlusion or shadowing (positive ρ_{pq}) inflates the variance of CRC — increasing the probability of all-visible or all-invisible events — but does not bias the expected value. Second, the independence of z_p and ΔR_p is conservative: a visible path (high SNR) tends to have smaller range residuals, so the true β_{match} given $z_p = 1$ is slightly larger than 0.852. Third, the range residual is summarised by a

single scalar; path-dependent range uncertainty, angular spread, and multipath clustering are not modelled.

A fourth limitation concerns the empirical calibration of $L_{\text{surrogate}}$. Standard monostatic radar in free space follows two-way path loss proportional to R^{-4} (-40 dB/decade). To characterise the NLOS attenuation regime of our scenes, we conducted a dedicated Sionna RT calibration study (333 ray-tracing calls across three room geometries at 24, 60, and 77 GHz). The measured total-scatter power slopes fall in the range -2 to -17 dB/decade — far shallower than free-space and substantially closer to R^{-2} (-20 dB/decade) than to R^{-4} (-40 dB/decade). The physical mechanism is room reverberation: multi-bounce reflections from walls, floor, and ceiling fill every delay window, so the observed scatter power at any distance is dominated by a diffuse energy floor rather than a clean single-bounce return. An R^{-2} surrogate fits the measured data with an RMSE of 13.1 dB/decade versus 32.5 dB/decade for R^{-4}. Our large-scale surrogate therefore adopts $L_{\text{surrogate}}(R_p) = R_p^{-2}$, strictly coupled with calibrated, frequency-dependent detection thresholds (`NLOS_THRESH_M`) derived from the ray-tracing oracle. This coupling makes $L_{\text{surrogate}}$ a *calibrated empirical proxy for detectability* rather than an exact free-space radar equation. Enforcing R^{-4} without recalibrating the material-specific thresholds disrupts this internal consistency and significantly degrades the CRC predictor's agreement with the oracle (Pearson r drops from 0.727 to 0.482).

Despite these simplifications, the agreement between predicted and measured CRC in Fig. 8 shows that the dominant mechanism is captured by the path-level detectability distribution.

This appendix completes the predictive chain from propagation physics to cross-modal correspondence rate, building on the SNR-to-CRC derivation of Appendix A:

$$\lambda \;\to\; \sigma_{\text{RCS}} \;\to\; P_{\text{rx}} \;\to\; \text{SNR} \;\to\; P_{\text{vis}} \;\to\; \text{CRC}.$$

The derivation assumes free-space monostatic propagation; the calibrated surrogate used for large-scale NLOS evaluation is described in Appendix A.4.

E. Radar Received Power with Wavelength Scaling

Under the monostatic radar equation, the received power for path p is:

$$P_{\text{rx}}(p, f) = \frac{P_t G_t G_r \lambda^2 \, \sigma_{\text{RCS}}(p, f)}{(4\pi)^3 R_p^4},$$

where $\lambda = c/f$ is the wavelength, $\sigma_{\text{RCS}}(p, f)$ is the effective radar cross section, and R_p is the round-trip path range. Grouping system constants into a factor C:

$$P_{\text{rx}}(p, f) = C \cdot \lambda^2 \cdot \sigma_{\text{RCS}}(p, f) \cdot R_p^{-4}.$$

F. Frequency Dependence of RCS

The effective RCS depends on the ratio of wavelength to object geometry. We model:

$$\sigma_{\text{RCS}}(p, f) \propto \lambda^{-\kappa_p},$$

where $\kappa_p \geq 0$ captures scattering behaviour: $\kappa_p \approx 0$ for specular reflectors (weak frequency dependence) and $\kappa_p \approx 2$ for diffuse or rough surfaces (strong frequency loss). Substituting:

$$P_{\text{rx}}(p, f) \propto \lambda^{2-\kappa_p} \cdot R_p^{-4}.$$

This explains why human-scattered paths (larger κ_p) degrade faster at high frequency, producing the CRC crossover observed in Figs. 2–3.

G. SNR in the dB Domain

Defining the per-path SNR in dB and substituting $\lambda = c/f$:

$$\text{SNR}_p^{\text{dB}}(f) = A_p - (2 - \kappa_p) \cdot 20 \log_{10}(f) - 40 \log_{10}(R_p),$$

where A_p absorbs system constants and mean scattering strength. Higher frequency reduces SNR when $\kappa_p > 2$; longer range causes rapid SNR decay at 40 dB/decade.

H. Closed-Form CRC Predictor

Substituting into the visibility model of Appendix A (Eq. (28)) and using the per-path SNR $s_p(f)$ derived in Section B.3, the expected-CRC formula becomes:

$$\boxed{\widehat{\text{CRC}}(f) = \frac{1}{K} \sum_{p \in \mathcal{P}_{\text{CSI}}^{(K)}} \Phi\big(\alpha\big(s_p(f) - \theta\big)\big)\,,} \tag{32}$$

where $s_p(f) = A_p - (2-\kappa_p) \cdot 20 \log_{10}(f) - 40 \log_{10}(R_p)$. This is the full physics-to-CRC mapping: CRC is a thresholded projection of wavelength-scaled, range-attenuated path energy.

Note on surrogate consistency. The $-40 \log_{10}(R_p)$ term reflects free-space R^{-4} propagation and captures the ideal physical scaling. The large-scale surrogate used for experimental validation employs a simplified R^{-2} model calibrated from Sionna RT measurements (Appendix A.4); the fitted parameters α and θ absorb this difference. This closed-form expression is provided for physical interpretability; direct numerical predictions should use the calibrated surrogate.

I. Origin of the Crossover Behaviour

The crossover arises when a path remains detectable at f_1 but falls below threshold at $f_2 > f_1$:

$$\Delta\text{SNR} = \text{SNR}(f_1) - \text{SNR}(f_2) \approx (2 - \kappa_p) \cdot 20 \log_{10}\left(\tfrac{f_2}{f_1}\right).$$

For $\kappa_p > 2$ (diffuse scatterer), $\Delta\text{SNR} > 0$: lower frequency has higher SNR, so lower frequency paths remain visible while higher frequency paths do not, directly producing the crossover. This establishes that CRC crossover is governed by κ_p (scattering roughness relative to wavelength), not by range resolution.

References

[1] Q. Pu, S. Jiang, and S. Gollakota, "Whole-home gesture recognition using wireless signals," vol. 43, no. 4. ACM New York, NY, USA, 2013, pp. 485–486.

[2] W. Wang, A. X. Liu, M. Shahzad, K. Ling, and S. Lu, "Understanding and modeling of wifi signal based human activity recognition," in *Proceedings of the 21st annual international conference on mobile computing and networking*, 2015, pp. 65–76.

[3] M. Kotaru, K. Joshi, D. Bharadia, and S. Katti, "Spotfi: Decimeter level localization using wifi," vol. 45, no. 4, 2015, pp. 269–282.

[4] F. Adib, Z. Kabelac, D. Katabi, and R. C. Miller, "3d tracking via body radio reflections," in *11th USENIX Symposium on Networked Systems Design and Implementation (NSDI 14)*, 2014, pp. 317–329.

[5] M. Zhao, T. Li, M. Abu Alsheikh, Y. Tian, H. Zhao, A. Torralba, and D. Katabi, "Through-wall human pose estimation using radio signals," in *Proceedings of the IEEE conference on computer vision and pattern recognition*, 2018, pp. 7356–7365.

[6] K. Qian, C. Wu, Z. Yang, Y. Liu, and K. Jamieson, "Widar: Decimeter-level passive tracking via velocity monitoring with commodity wi-fi," in *Proceedings of the 18th ACM international symposium on mobile ad hoc networking and computing*, 2017, pp. 1–10.

[7] Y. Xie, J. Xiong, M. Li, and K. Jamieson, "md-track: Leveraging multi-dimensionality in passive indoor wi-fi tracking," in *The 25th Annual International Conference on Mobile Computing and Networking*, 2019, pp. 1–16.

[8] F. Adib, H. Mao, Z. Kabelac, D. Katabi, and R. C. Miller, "Smart homes that monitor breathing and heart rate," in *Proceedings of the 33rd annual ACM conference on human factors in computing systems*, 2015, pp. 837–846.

[9] J. Sanson, R. C. Shah, M. Pinaroc, and V. Frascolla, "Extracting range-doppler information of moving targets from wi-fi channel state information," *arXiv preprint arXiv:2508.02799*, 2025.

[10] J. Sanson, R. C. Shah, M. Pinaroc, C. Tanriover, and V. Frascolla, "Livesense: A real-time wi-fi sensing platform for range-doppler on cots laptop," *arXiv preprint arXiv:2603.06545*, 2026.

[11] J. Sanson, R. C. Shah, and V. Frascolla, "Human presence detection via wi-fi range-filtered doppler spectrum on commodity laptops," *arXiv preprint arXiv:2603.10845*, 2026.

[12] X. Chen and X. Zhang, "RF Genesis: Zero-shot generalization of mmwave sensing through simulation-based data synthesis and generative diffusion models," in *Proceedings of the 21st ACM Conference on Embedded Networked Sensor Systems*, 2023, pp. 28–42.

[13] F. A. Aoudia, J. Hoydis, M. Nimier-David, B. Nicolet, S. Cammerer, and A. Keller, "Sionna rt: Technical report," *arXiv preprint arXiv:2504.21719*, 2025.

[14] Remcom, "Wireless InSite propagation simulation software," https://www.remcom.com/wireless-insite, accessed 2025.

[15] M. I. Skolnik, *Introduction to Radar Systems*, 3rd ed. McGraw-Hill, 2001.

[16] T. Dogaru and C. Le, "Validation of Xpatch computer models for human body radar signature," *US Army Research Laboratory Technical Report ARL-TR-4403*, 2008.